Progress In Electromagnetics Research C, Vol. 172, 252–261, 2026

PIER C

(Received 30 June 2026, Accepted 29 July 2026, Scheduled 10 August 2026)

Design and Characteristic Analysis of Radial Four-Pole Three-Degree-of-Freedom Hybrid Magnetic Bearing with Axial Auxiliary Electric Excitation

Xiaoting Ye*, Xianhai Yu, Zirui Chen, and Tao Zhang

Faculty of Automation, Huai'an University, Huai'an 223003, China

ABSTRACT: This study presents a novel three-degree-of-freedom (3-DOF) axial-enhanced hybrid magnetic bearing (AEHMB), which introduces an axial auxiliary electric excitation to break the inherent proportional constraint between radial and axial maximum suspension forces in conventional 3-DOF HMBs. This configuration enables independent design of radial and axial bearing performance, satisfying diverse application demands in transmission systems while effectively enhancing axial load-bearing capability. This study first elaborates the structural topology of the proposed 3-DOF AEHMB, along with its primary bias magnetic circuit and axial compensation bias magnetic circuit. Mathematical models for the axial and radial suspension forces are subsequently established based on equivalent magnetic circuit analysis. Based on the maximum design requirements for radial and axial suspension forces, key structural parameters were optimized and determined. Finally, the finite element method was adopted to validate the rationality of the magnetic circuit configuration and suspension working mechanism through systematic calculations of the air-gap bias flux density, control flux density, force-current characteristics, and force-displacement characteristics. Simulation results verified the feasibility of the proposed structure, accuracy of the magnetic circuit design method and mathematical models, and reliability of the overall design scheme for the 3-DOF AEHMB.

1. INTRODUCTION

Magnetic bearings (MBs) represent a class of high-performance non-contact supporting devices that suspend rotors at the geometric center of the stators by exploiting suspension forces between stator and rotor components. In stark contrast to conventional mechanical bearings, MBs exhibit distinct advantages, including friction-free operation, lubrication-free maintenance, tunable stiffness and damping characteristics, extended service life, and remarkably low power loss. Benefiting from these exceptional superiorities, MBs have gained widespread deployment in a broad spectrum of high-end scenarios, ranging from aerospace systems, high-speed eddy-current molecular pumps, high-speed motorized spindles, to ultra-clean industrial environment [1–5].

Typical MB topologies can be categorized into passive magnetic bearings (PMBs), active magnetic bearings (AMBs), and HMBs [6–11]. Among these configurations, HMBs integrate the respective advantages of PMBs and AMBs. Distinct from AMBs, which rely entirely on bias currents to establish static bias magnetic fields, HMBs use permanent magnets to generate an inherent bias flux, and dedicated suspension windings are deployed to produce dynamically controlled magnetic fields. The superposition of the bias and control magnetic fields yields a stable suspension force for the rotor support [12, 13]. As a result, HMBs can effectively decrease power amplifier consumption, reduce the required number of coil turns, and minimize system volume and weight, while simultaneously improving suspension force density, which has established them as a mainstream research focus in the MB community. According to the number of controllable degrees of freedom, HMBs can be further classified into 1-DOF axial, 2-DOF radial, and 3-DOF radial-axial HMBs [14–19]. The 3-DOF radial-axial HMB integrates radial and axial suspension functions into a single compact unit and is capable of providing radial and axial suspension forces simultaneously. When deployed in high-speed motors, 3-DOF HMB can effectively shorten the overall axial length, elevate the critical speed, and enhance both the suspension force and power densities. For these reasons, diverse structural designs of 3-DOF radial-axial HMBs have been extensively investigated by researchers worldwide.

Currently, MBs are undergoing accelerated development toward high-speed and high-power operating scenarios. In high-speed fan systems, the rotation of blades generates considerable axial aerodynamic pressure, making the axial load far exceed the radial load and thus rendering axial bearing performance a critical design priority for such equipment [20–22]. 3-DOF HMBs, owing to their compact topology, high structural stiffness, and low power loss, are particularly well-suited for high-speed air compressor applications [23, 24]. To improve flux utilization efficiency, conventional 3-DOF HMBs adopt a shared magnetic circuit topology where the permanent magnet flux passes through both the axial and radial air gaps. Although this design minimizes the 3-DOF HMB size, it imposes equal total magnetic flux on the radial and axial air gaps. Under the condition of saturated and identical air-gap flux density, the total area of the radial poles must be strictly equal to that of the

* Corresponding author: Xiaoting Ye (yxthyit@hyit.edu.cn).

axial poles. This inherent constraint leads to a fixed proportional relationship between the axial and radial maximum suspension forces, which severely limits the flexibility of structural design. In particular, the traditional four-pole 3-DOF HMB has a constant ratio of 2.0 for its maximum achievable suspension force between the axial and radial directions, and this relationship cannot be adaptively adjusted based on actual operational requirements [25–28].

To address these limitations, this study proposes a novel four-pole 3-DOF HMB. The proposed design maximizes the utilization of the axial pole areas and fundamentally breaks the inherent proportional constraint between the radial and axial maximum suspension forces. Under the premise of maintaining unchanged radial maximum suspension forces, the axial-to-radial load ratio can be flexibly enhanced to 3.0 or even 4.0 based on practical design requirements.

2. STRUCTURE AND PRINCIPLE

2.1. The Structure of 3-DOF AEHMB

The three-dimensional structural configuration of the proposed four-pole 3-DOF AEHMB is illustrated in Figure 1. Based on the conventional 3-DOF HMB topology, an additional L-shaped auxiliary outer stator was integrated, and a dedicated constant-current excitation winding was embedded to fully utilize the axial pole area and substantially enhance the axial bias magnetic flux. The radially magnetized permanent magnet ring supplies the entire radial bias flux, as well as a portion of the axial bias flux, and the remaining required axial bias flux is supplemented by energizing the constant-current winding.

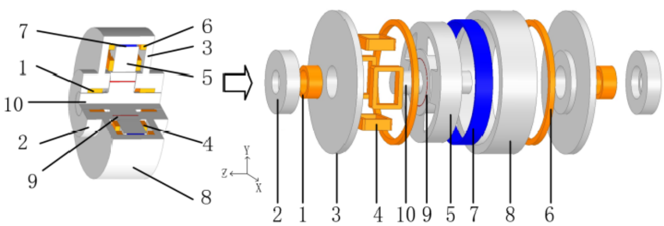

FIGURE 1. Structure of the 3-DOF AEHMB. (1) Constant current source winding, (2) L-type auxiliary outer stator, (3) axial stator piece, (4) radial control coils, (5) radial stator, (6) axial control coils, (7) radial magnetized permanent magnet ring, (8) axial stator ring, (9) aluminum ring, and (10) rotor.

The proposed 3-DOF AEHMB mainly consists of an axial stator, two L-shaped auxiliary outer stators, a radial stator, axial control coils, radial control coils, constant-current excitation windings, a radially magnetized permanent magnet ring, a magnetic isolation ring, and a rotor. A sintered Nd-Fe-B radially magnetized permanent magnet ring was arranged between the radial stator poles and the axial stator ring. The radial control coils were wound around the poles of the radial stator, and a constant-current excitation winding was installed inside the internal groove of the L-shaped auxiliary outer stator. Furthermore, a magnetic isolation ring is embedded on the rotor to isolate the bias magnetic flux generated by both the permanent magnet ring and constant-current winding, thereby preventing magnetic flux interference.

2.2. Working Principle of 3-DOF AEHMB

The cyan dotted lines in Figure 2(a) illustrate the bias flux generated by the permanent magnet ring. Originating from the N pole of the permanent magnet ring, the flux splits into two symmetrical branches at the outer axial stator. These two branches then sequentially traverse the bilateral axial air gaps, axial stator poles, outer rotor region of the magnetic isolation ring, and radial air gap, and finally converge at the radial stator poles before returning to the S pole of the permanent magnet ring, thereby forming a completely closed magnetic circuit. The purple dotted lines in Figure 2(a) represent the bias flux generated by the constant-current excitation winding. This flux originates from the L-shaped auxiliary stator, passes through the axial bias air gap and inner rotor region of the magnetic isolation ring, and forms an independent closed magnetic loop. The left and right constant-current windings are energized in opposite directions to ensure that the generated bias flux superposes the permanent magnet bias flux in the same direction. The black solid lines in Figure 2(a) denote the axial control flux generated by the axial control winding. The flux emanates from the outer axial stator and is divided into three distinct branches at the axial air gap. The first two branches penetrate the rotor through the outer and inner sides of the magnetic isolation ring, respectively, and converge at the opposite axial air gap before returning to the axial direction of the stator. The third branch corresponds to a small amount of leakage flux, which infiltrates the rotor through the unilateral bias air gap, merges with the other two branches at the axial stator yoke, and finally flows back to the outer axial stator yoke.

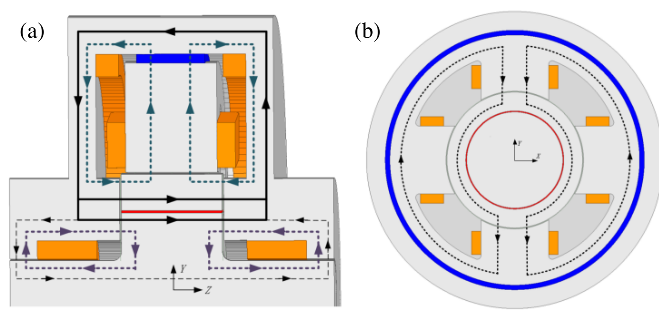

FIGURE 2. Magnetic circuit of 3-DOF AEHMB. (a) The overall axial magnetic circuit and (b) the magnetic circuit with radial flux control.

The dashed lines in Figure 2(b) represent the radial control flux generated by the radial control winding. The flux emanates from a single radial stator pole, penetrates the radial air gap and rotor, and reaches the opposite radial stator pole. It then splits into two sub-branches inside the radial stator yoke and eventually returns to the initial pole, forming a fully closed radial magnetic circuit.

The permanent magnet bias flux simultaneously penetrates the outer axial and radial air gaps outside the magnetic isolation ring, maintaining the flux density in both air gaps at half the saturation value. Meanwhile, the inner axial air gap also operates at a half-saturated flux density provided by the excited constant-current winding. Under steady suspension conditions, the cooperative excitation of the permanent magnet ring and the constant-current winding establishes a stable bias magnetic

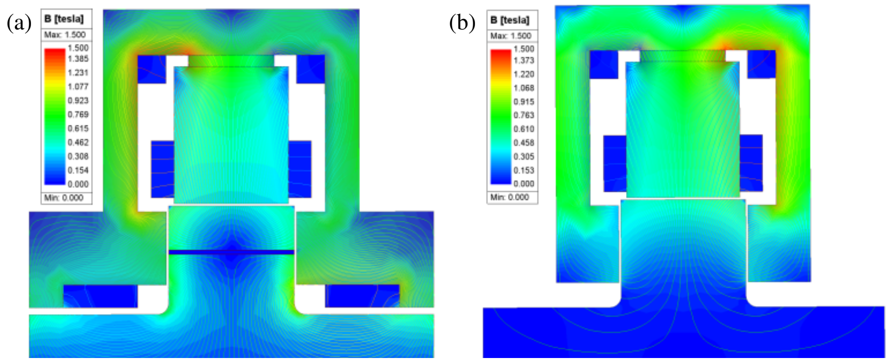

FIGURE 3. Comparison diagram of axial air-gap magnetic density. (a) 3-DOF AEHMB and (b) 3-DOF HMB.

field to maintain the force balance and stable suspension of the rotor. When external disturbances cause rotor displacement, regulated currents are injected into the corresponding control windings to realize a precise position adjustment in either the axial or radial direction.

During axial regulation, the control flux generated by the energized axial control winding penetrates both the inner and outer regions of the rotor's magnetic isolation ring. This flux positively superposes the bias flux on one side and counteracts it on the other side. This distinctive working mechanism effectively enlarges the equivalent effective area of the axial magnetic poles and significantly improves the ultimate axial maximum suspension force of the proposed 3-DOF AEHMB.

Figure 3 compares the axial magnetic flux density distributions of the proposed 3-DOF AEHMB and conventional 3-DOF HMB. As illustrated in Figure 3(b), the conventional 3-DOF HMB exhibits a higher axial flux density near the radial stator side but a lower flux density near the rotor shaft. This uneven distribution restricts the improvement of the axial controllable bearing capacity. In contrast, the proposed 3-DOF AEHMB adopts a magnetic barrier ring to segment the axial magnetic poles, as shown in Figure 3(a). By optimizing the installation position of the magnetic barrier ring, the outer axial air gap maintains a stable flux density at half the saturation value. Meanwhile, the flux density of the inner axial air gap in the magnetic barrier ring was independently provided by the constant-current excitation winding, which was also set to half of the saturated air-gap flux density. The comparative results demonstrate that the proposed design effectively eliminates the low-flux-density region near the rotor shaft, improves the utilization rate of the axial magnetic poles, and ultimately enhances the overall axial maximum suspension force.

3. ANALYSIS OF THE 3-DOF AEHMB

To improve the controllable axial maximum suspension force and break the inherent proportional constraint between the axial and radial maximum suspension forces in the conventional 3-DOF HMB, this section establishes an equivalent magnetic circuit model of the proposed 3-DOF AEHMB. The model focuses on the axial flux to realize the flexible regulation of the axial and radial maximum suspension forces.

3.1. The Equivalent Magnetic Circuit Model

To simplify theoretical calculation, a mathematical model of the proposed 3-DOF AEHMB was established based on the equivalent magnetic circuit method. In this modeling process, nonlinear factors, including magnetic reluctance, eddy current loss, fringing effect, temperature variation, and magnetic saturation of ferromagnetic materials, were reasonably ignored. A schematic of the established equivalent bias magnetic circuit is shown in Figure 4.

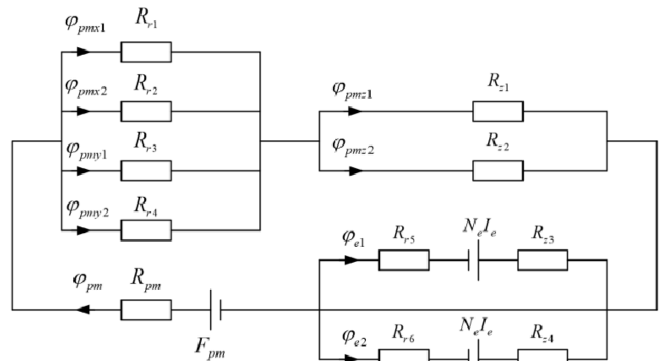

FIGURE 4. Equivalent bias magnetic circuit diagram.

Figure 4 shows the equivalent bias magnetic circuit. Specifically, φ_{pm} denotes the total bias flux generated by the permanent magnet ring; φ_{pmx1} and φ_{pmx2} represent the bias fluxes across the radial X-direction rotor air gaps; φ_{pmy1} and φ_{pmy2} denote the bias fluxes across the radial Y-direction rotor air gaps; φ_{pmz1} and φ_{pmz2} indicate the bias fluxes at the outer axial air gaps outside the rotor magnetic barrier ring; and φ_{e1} and φ_{e2} correspond to the bias fluxes at the inner axial air gaps inside the rotor magnetic barrier ring.

The magnetic reluctance of the permanent magnet ring can be formulated as follows:

$$R_{pm} = \frac{L_{pm}}{\mu_{pm} S_{pm}} \tag{1}$$

where L_{pm} is the radial magnetization length of the permanent magnet ring; μ_{pm} is the magnetic permeability of the permanent magnet material; and S_{pm} is the effective cross-sectional area of the permanent magnet ring in the magnetic circuit. When the rotor produces displacement offsets of Δx, Δy, and Δz along the 3-DOF, the magnetic reluctance of each air gap can be expressed as follows:

$$\begin{cases} R_{r1}=\frac{\delta_r-\Delta x}{\mu_0 S_r}, & R_{z1}=\frac{\delta_z-\Delta z}{\mu_0 S_{zout}} \\ R_{r2}=\frac{\delta_r+\Delta x}{\mu_0 S_r}, & R_{z2}=\frac{\delta_z+\Delta z}{\mu_0 S_{zout}} \\ R_{r3}=\frac{\delta_r-\Delta y}{\mu_0 S_r}, & R_{z3}=\frac{\delta_z-\Delta z}{\mu_0 S_{zin}} \\ R_{r4}=\frac{\delta_r+\Delta y}{\mu_0 S_r}, & R_{z4}=\frac{\delta_z+\Delta z}{\mu_0 S_{zin}} \\ R_{r5}=\frac{\delta_r-\Delta r}{\mu_0 S_{re}}, & R_{r6}=\frac{\delta_r+\Delta r}{\mu_0 S_{re}} \end{cases} \tag{2}$$

where $R_{r1}\sim R_{r4}$ are air-gap reluctances of the four radial magnetic poles; R_{r5} and R_{r6} are air-gap reluctances of the auxiliary axial stator; R_{z1} and R_{z2} correspond to axial air-gap reluctances between the axial stator and the outer magnetic barrier ring of the rotor; R_{z3} and R_{z4} denote axial air-gap reluctances between the axial stator and the inner magnetic barrier ring of the rotor. Moreover, δ_r is the equilibrium working length of the radial air gap; μ is the vacuum permeability; and S_r is the area of the radial magnetic pole. Similarly, δ_z denotes the equilibrium working length of the axial air gap; S_{zout} is the overlapping area between the outer side of the rotor magnetic barrier ring and the outer axial stator; S_{re} refers to the radial projection area of the rotor on the L-shaped auxiliary stator; and S_{zin} represents the opposite area between the inner side of the rotor magnetic barrier ring and the axial stator.

The total reluctance of the bias flux loop R_{sum} consists of three components: the total radial air-gap reluctance R_{rsum}, the total outer axial air-gap reluctance of the rotor barrier ring R_{zsum}, and the reluctance of the permanent magnet ring R_m. Accordingly, R_{sum} can be mathematically expressed as follows:

$$R_{sum}=R_{rsum}+R_{zsum}+R_m \tag{3}$$

where R_{rsum} and R_{zsum} respectively represent:

$$R_{rsum} = 1/[1/R_{r1}+1/R_{r2}+1/R_{r3}+1/R_{r4}] \tag{4}$$

$$R_{zsum} = 1/[1/R_{z1}+1/R_{z2}] \tag{5}$$

The magnetic motive force F_{pm} of the permanent magnet ring is shown as follows:

$$F_{pm}=H_c L_{pm} \tag{6}$$

where H_c is the coercive force of the permanent magnet material.

According to the magnetic circuit diagram shown in Figure 4, the radial bias magnetic flux φ_{pmx1}, φ_{pmx2}, φ_{pmx3}, φ_{pmx4} can be expressed as

$$\begin{cases} \varphi_{pmx1}=\lambda_{pm}\frac{F_{pm}R_{rsum}}{R_{sum}R_{r1}}, & \varphi_{pmx2}=\lambda_{pm}\frac{F_{pm}R_{rsum}}{R_{sum}R_{r2}} \\ \varphi_{pmy1}=\lambda_{pm}\frac{F_{pm}R_{rsum}}{R_{sum}R_{r3}}, & \varphi_{pmy2}=\lambda_{pm}\frac{F_{pm}R_{rsum}}{R_{sum}R_{r4}} \end{cases} \tag{7}$$

where λ_{pm} is the flux leakage coefficient for the pole air gap corresponding to the bias flux produced by the permanent magnet ring, with a typical empirical value ranging from 0.9 to 0.95.

The axial bias fluxes φ_{pmz1} and φ_{pmz2} are defined as follows:

$$\left\{ \varphi_{pmz1}=\lambda_{pm}\frac{F_{pm}R_{zsum}}{R_{sum}R_{z1}}, \quad \varphi_{pmz2}=\lambda_{pm}\frac{F_{pm}R_{zsum}}{R_{sum}R_{z2}} \right. \tag{8}$$

The compensated bias flux φ_{e1} generated by the constant-current source winding is expressed as follows:

$$\varphi_{e1}=\lambda_{NI}\frac{N_e I_e}{R_{z3}+R_{r5}}; \quad \varphi_{e2}=\lambda_{NI}\frac{N_e I_e}{R_{z4}+R_{r6}} \tag{9}$$

where λ_{NI} represents the magnetic leakage coefficient of the control winding at the pole air gap, usually 0.9–0.95.

The equivalent control magnetic circuit diagram of the 3-DOF AEHMB is presented in Figure 5. Specifically, $N_r I_x$, $N_r I_y$, and $N_r I_z$ denote the magnetomotive forces produced by the radial X-direction, radial Y-direction, and axial control windings, respectively. The control fluxes generated by the radial X- and Y-direction windings are represented by φ_{x1}, φ_{x2} and φ_{y1}, φ_{y2}, respectively. For the axial control winding, φ_{zou} and φ_{zin} correspond to the control fluxes at the outer and inner axial air gaps of the rotor magnetic barrier ring, respectively, whereas φ_{zleak} is the leakage flux formed at the radial air gap between the rotor and the L-shaped outer stator. To reduce the computational complexity, the magnet reluctance R_m in the relevant formulas was approximated to zero, and the axial control flux model was reasonably simplified.

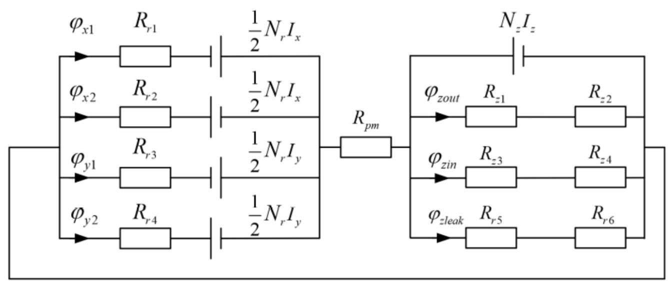

FIGURE 5. Equivalent control flux magnetic circuit diagram.

According to the magnetic circuit diagram depicted in Figure 5, the radial control flux φ_{x1}, φ_{x2}, φ_{y1}, φ_{y2} can be mathematically described as follows:

$$\begin{cases} \varphi_{x1}=\varphi_{x2}=\lambda_{NI}\frac{N_r I_x}{R_{r1}+R_{r2}} \\ \varphi_{y1}=\varphi_{y2}=\lambda_{NI}\frac{N_r I_y}{R_{r3}+R_{r4}} \end{cases} \tag{10}$$

The simplified mathematical equations for the axial control fluxes φ_{zout}, φ_{zin}, and φ_{zleak} are as follows:

$$\begin{cases} \varphi_{zout}=\lambda_{NI}\frac{N_z I_z}{R_{z1}+R_{z2}} \\ \varphi_{zin}=\lambda_{NI}\frac{N_z I_z}{R_{z3}+R_{z4}} \\ \varphi_{zleak}=\lambda_{NI}\frac{N_z I_z}{R_{r5}+R_{r6}} \end{cases} \tag{11}$$

3.2. Expression of Suspension Forces

At present, the control and bias fluxes have been acquired at the operational air gap, enabling derivation of the suspension force equation via the superimposition of the air-gap flux. The

TABLE 1. The stiffness coefficients.

Item	Value
K_{ix}	$\dfrac{\lambda_{pm}H_cL_{pm}\lambda_{NI}N_r}{\delta_r\left(\dfrac{\delta_r}{4\mu_0S_r}+\dfrac{\delta_z}{2\mu_0S_{zout}}+\dfrac{L_{pm}}{\mu_{pm}S_{pm}}\right)}$
K_{dx}	$\dfrac{\lambda_{pm}^2H_c^2L_{pm}^2}{8\mu_0\delta_rS_r\left(\dfrac{\delta_r}{4\mu_0S_r}+\dfrac{\delta_z}{2\mu_0S_{zout}}+\dfrac{L_{pm}}{\mu_{pm}S_{pm}}\right)^2}$
K_{iy}	$\dfrac{\lambda_{pm}H_cL_{pm}\lambda_{NI}N_r}{\delta_r\left(\dfrac{\delta_r}{4\mu_0S_r}+\dfrac{\delta_z}{2\mu_0S_{zout}}+\dfrac{L_{pm}}{\mu_{pm}S_{pm}}\right)}$
K_{dy}	$\dfrac{\lambda_{pm}^2H_c^2L_{pm}^2}{8\mu_0\delta_rS_r\left(\dfrac{\delta_r}{4\mu_0S_r}+\dfrac{\delta_z}{2\mu_0S_{zout}}+\dfrac{L_{pm}}{\mu_{pm}S_{pm}}\right)^2}$
K_{iz}	$\dfrac{\lambda_{pm}H_cL_{pm}\lambda_{NI}N_z}{2\delta_r\left(\dfrac{\delta_r}{4\mu_0S_r}+\dfrac{\delta_z}{2\mu_0S_{zout}}+\dfrac{L_{pm}}{\mu_{pm}S_{pm}}\right)}+\dfrac{\lambda_{NI}^2N_eI_eN_z}{\delta_z\left(\dfrac{\delta_z}{\mu_0S_{zin}}+\dfrac{\delta_r}{\mu_0S_{re}}\right)}$
K_{dz}	$\dfrac{\lambda_{pm}^2H_c^2L_{pm}^2}{2\mu_0\delta_zS_{zout}\left(\dfrac{\delta_r}{4\mu_0S_r}+\dfrac{\delta_z}{2\mu_0S_{zout}}+\dfrac{L_{pm}}{\mu_{pm}S_{pm}}\right)^2}+\dfrac{2\lambda_{NI}^2N_e^2I_e^2}{\mu_0^2S_{zin}^2\left(\dfrac{\delta_r}{\mu_0S_{re}}+\dfrac{\delta_z}{\mu_0S_{zin}}\right)^3}$

suspension force equation is as follows:

$$\begin{aligned}
F_x &= \frac{(\varphi_{pmx1}+\varphi_{x1})^2}{2\mu_0S_r}-\frac{(\varphi_{pmx2}-\varphi_{x2})^2}{2\mu_0S_r}\\
F_y &= \frac{(\varphi_{pmy1}+\varphi_{y1})^2}{2\mu_0S_r}-\frac{(\varphi_{pmy2}-\varphi_{y2})^2}{2\mu_0S_r}\\
F_z &= \frac{(\varphi_{pmz1}+\varphi_{zout})^2}{2\mu_0S_{zout}}+\frac{(\varphi_{e1}+\varphi_{zin})^2}{2\mu_0S_{zin}}\\
&\quad-\frac{(\varphi_{pmz2}-\varphi_{zout})^2}{2\mu_0S_{zout}}+\frac{(\varphi_{e2}-\varphi_{zin})^2}{2\mu_0S_{zin}}
\end{aligned}\tag{12}$$

By linearizing the suspension forces F_x and F_y, as well as the axial suspension force F_z, around the equilibrium position and omitting infinitesimal quantities higher than the second order, the corresponding current stiffness coefficients K_{ix}, K_{iy}, K_{iz} and displacement stiffness coefficients K_{dx}, K_{dy}, K_{dz} can be derived.

$$\begin{aligned}
F_x &\approx \left.\frac{\partial F_x}{\partial\Delta_x}\right|_{\Delta x=0}^{i_x=0}\cdot x+\left.\frac{\partial F_x}{\partial i_x}\right|_{\Delta x=0}^{i_x=0} i_x = K_{dx}\cdot x+K_{ix}\cdot i_x\\
F_y &\approx \left.\frac{\partial F_y}{\partial\Delta_y}\right|_{\Delta y=0}^{i_y=0}\cdot y+\left.\frac{\partial F_y}{\partial i_y}\right|_{\Delta y=0}^{i_y=0} i_y = K_{dy}\cdot y+K_{iy}\cdot i_y\\
F_z &\approx \left.\frac{\partial F_z}{\partial\Delta_z}\right|_{\Delta z=0}^{i_z=0}\cdot z+\left.\frac{\partial F_z}{\partial i_z}\right|_{\Delta z=0}^{i_z=0} i_z = K_{dz}\cdot z+K_{iz}\cdot i_z
\end{aligned}\tag{13}$$

The stiffness coefficient directly reflects the maximum suspension force of the 3-DOF AEHMB. Higher values of K_{dx}, K_{dy}, K_{dz} correspond to smaller displacement of the rotor from its equilibrium position for the same suction force. The control current required to generate the same suspension force decreased as the values of K_{ix}, K_{iy}, K_{iz} increased. Table 1 reveals a direct correlation between the magnetomotive force F_{pm} of the permanent magnet ring and the reduced control current or displacement required to achieve an equivalent bearing capacity of the levitated load. By summing the two terms, we obtained the axial current and displacement stiffness coefficients for the designed 3DOF AEHMB. In contrast, in the conventional 3-DOF HMB depicted in Figure 3(b), only one term preceding the plus sign in this table represents its axial current stiffness coefficient and displacement stiffness coefficient. The design incorporates a constant current source winding to compensate for the axial bias magnetic flux, thereby effectively enhancing the axial bias magnetomotive force (MMF). This results in improved axial stiffness coefficients K_{iz} and K_{dz}, increased capacity for the axial control bearing, and enhanced sensitivity of the axial control current.

4. PARAMETER DESIGN AND SIMULATION VERIFICATION

According to design requirements, the 3DOF AEHMB designed in this study was required to achieve a radial suspension force of 300 N and an axial suspension force of 900 N. To validate the correctness of the suspension force calculation formula derived in this paper, three-dimensional finite element modeling and simulation were conducted on the 3DOF AEHMB model. The model parameters are presented in Table 2.

4.1. The Main Parameter Design of 3-DOF AEHMB

4.1.1. Determine the Radial Magnetic Pole Area

Assume that the maximum suspension force is generated along the X-axis and that the rotor offsets Δx, Δy, and Δz equal to zero. When the maximum current I_{xmax} is applied to the radial X-direction control winding, the magnetic flux density at the air gap of radial magnetic pole 2 in Figure 2(b) diminishes to zero, while that at the air gap of radial magnetic pole 4 doubles and reaches the saturated air-gap bias magnetic density. Consequently, the following relationship can be derived:

$$F_{xmax}=\frac{4\varphi_{pmx1}^2}{2\mu_0S_r}=\frac{(B_{rmax}S_r)^2}{2\mu_0S_r}=\frac{B_{rmax}^2S_r}{2\mu_0}\tag{14}$$

In this design, the radial maximum suspension force F_{xmax} is 300 N; the radial saturation magnetic induction intensity B_{rmax} is set to 1.2 T; and the air permeability is a constant, namely $\mu=4\pi\times10^{-7}$ H/m, from which the radial magnetic pole area S_r can be calculated.

4.1.2. Determine the External Axial Pole Area S_{zout}

According to the bias flux path generated by the permanent magnet ring, the bias flux of the radial and axial air gaps can be obtained as follows:

$$2B_{zout0}S_{zout}=4B_{r0}S_r\tag{15}$$

TABLE 2. 3 DOF-AEHMB model parameters.

Parameter	Value	Unit
Outer diameter of stator shell	63.4	mm
Inner diameter of stator shell	55.4	mm
Outer diameter of rotor thrust disc	29	mm
Inside diameter of rotating shaft	10	mm
Residual magnetic induction	0.6	T
Radial air gap length δ_r	0.4	mm
Axial air gap length δ_z	0.4	mm
Radial air gap length of L-shaped outer stator δ_{re}	1.2	mm
Coercive force of permanent magnet ring H_c	700000	A/m
Magnetizing length of permanent magnet ring L_{pm}	2	mm
Radial pole cross-sectional area S_r	580	mm^2
Axial outward magnetic pole area S_{zout}	1386	mm^2
Axial internal magnetic pole area S_{zin}	530	mm^2
Number of turns in radial winding N_x	180	/
Number of turns in axial winding N_z	180	/
Numbers of constant current source winding N_e	360	/

The bias flux densities B_{zout0} and B_{r0}, both equal to 0.6 T, represent the respective magnetic flux density at the air gaps of the external axial and radial magnetic poles. Consequently, it becomes possible to determine the area S_{zout} of the axial magnetic pole outside the rotor's magnetic barrier ring.

4.1.3. Determine the Internal Axial Pole Area S_{zin}

When the maximum axial suspension force is generated with rotor offsets Δx, Δy, and Δz equal to 0 and by passing the maximum control current I_{zmax} into the axial control winding, we can derive the following expression for the axial maximum suspension force:

$$F_{zmax} = \frac{(2\varphi_{pmz1})^2}{2\mu_0 S_{zout}} + \frac{(2\varphi_{e1})^2}{2\mu_0 S_{zin}} = \frac{B_{zmax}^2(S_{zout}+S_{zin})}{2\mu_0} \tag{16}$$

The axial saturation magnetic flux density, denoted as B_{zmax}, is equivalent to the radial saturation magnetic flux density of 1.2 T. Based on the aforementioned formula, the internal axial magnetic pole area S_{zin} can be determined.

4.1.4. Determine the Magnetomotive Force FPM

In Subsection 1, the radial magnetic pole area S_r was obtained. Assuming that the offset of rotor Δx, Δy, and Δz in three directions are 0, the magnetomotive force F_{pm} of the permanent magnet ring can be obtained according to equation $B_{rmax}S_r = 2\varphi_{pmx1}$.

4.1.5. Determine the Ampere-Turns NEIE of Constant Current Source Winding

When the rotor offsets in 3-DOFs are 0, the bias flux generated by the constant current source winding is stored in the following equation:

$$\varphi_{e1} = \varphi_{e2} = \lambda_{NI}\frac{N_e I_e}{R_{z3}+R_{r5}} = B_{zmax}S_{zin} \tag{17}$$

According to the above formula, the minimum ampere-turns N_eI_e of the constant current source winding can be obtained under the premise that the axial bearing capacity F_{zmax} is satisfied.

4.1.6. Parameter Design Results

Based on the above analysis, the final design parameters of the 3-DOF AEHMB are listed in Table 2.

4.2. DOF-AEHMB Magnetic Field Distribution

Figure 6(a) illustrates the magnetic flux density curve at the radial air gap when the control current is not applied, and only the constant current source winding is energized. Here, the horizontal axis represents the circular angle starting from the positive direction of the Z-axis in a clockwise manner, and the vertical axis indicates the bias magnetic flux density at the radial air gap. Numbers 1–4 correspond to the magnetic flux density at the corresponding air-gap locations of the pole faces in Figure 2. When the current through the constant current source winding $I_{Enhance} = 0$ A, it indicates that there is no current in the constant current source winding and the air-gap magnetic flux is entirely generated by the permanent magnet ring. At this time, the magnetic flux densities at the four pole-face air gaps were 0.6 T. When the current through the constant current source winding $I_{Enhance}$ gradually increases, the radial air-gap magnetic flux density has almost no change. It can be observed that the constant current source winding has almost no effect on the magnetic flux density at the radial pole face air gap when it

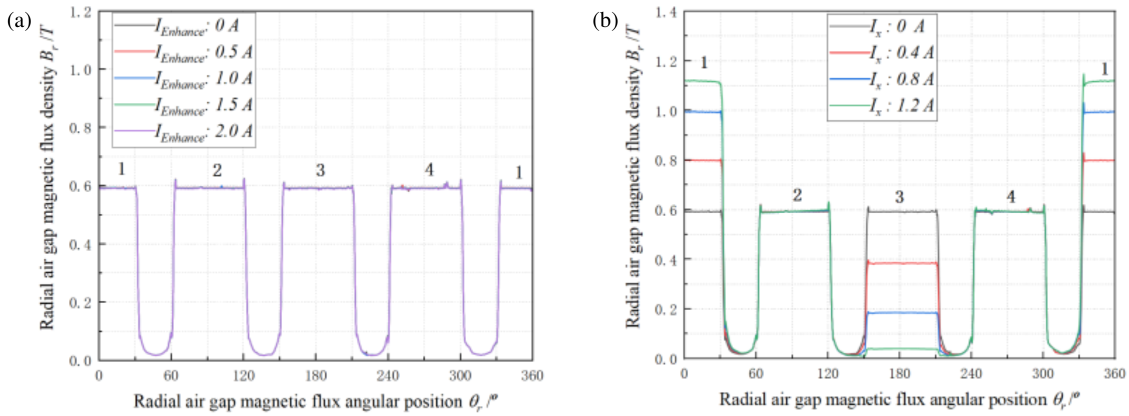

FIGURE 6. Radial air-gap flux density map for different current passing through the winding. (a) The radial air-gap magnetic flux density variation curve of the current source winding when different currents are passed through it. (b) The radial flux density variation curve of the radially controlled winding with different current flow.

is supplied with different currents, which is consistent with the relationship in the radial stiffness coefficient expression, proving that the existence of the constant current source winding does not affect the radial bearing capacity.

The magnetic flux density of the radially controlled winding at the air gap of each pole, when different currents are applied, is shown in Figure 6(b), with labels 1–4 corresponding to the magnetic flux density at the air gap of each pole in Figure 3. When the control current I_x is 0 A, the air-gap magnetic flux density is entirely generated by the permanent magnet ring, with the magnetic flux densities of the four pole air gaps being 0.6 T. As the control current I_x gradually increases, the magnetic flux density at the air gap of pole 1 increases, and the magnetic flux density at the air gap of pole 3 decreases, with the magnetic flux density at the air gaps of poles 2 and 4 remaining approximately constant. When $I_x = 1.2$ A, the air gap magnetic flux density at pole 3 is close to zero, and the radial bearing capacity theoretically approaches its highest value. The magnetic-field distribution of the structure is shown in Figure 7.

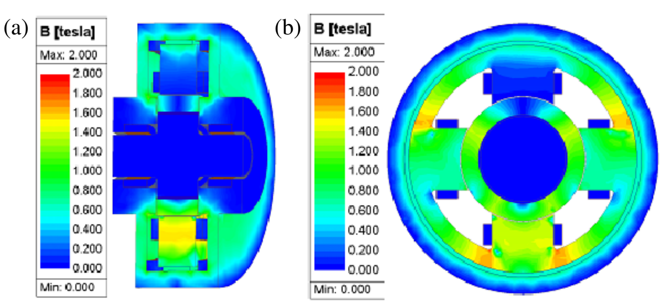

FIGURE 7. Radial current $I_x = 1.2$ A radial magnetic flux density map. (a) 3-DOF-AEHMB axial view and (b) 3-DOF-AEHMB radial view.

The 3-DOF AEHMB proposed in this study adopts an auxiliary constant-current winding to compensate for the axial bias flux to improve the axial bearing capacity. Finite element simulation software was used to analyze the magnetic flux density distribution at the axial air gap, as illustrated in Figure 8. The thick black curve spanning between the two arrows denotes the air-gap flux density under various operating currents with the compensation winding unexcited $I_z = 0$ A.

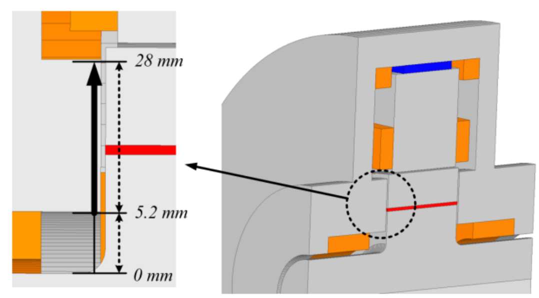

FIGURE 8. Axial air-gap structure details diagram.

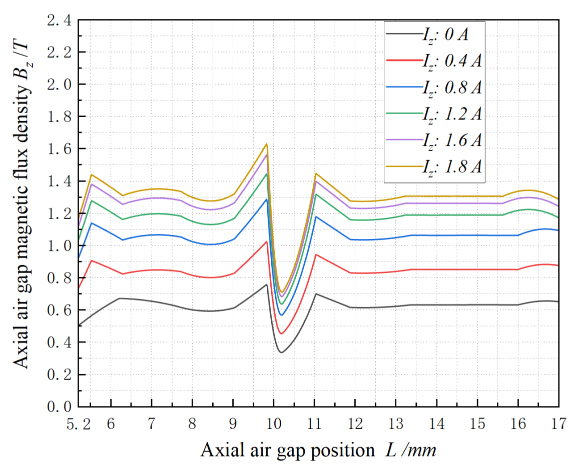

FIGURE 9. Magnetic flux density curves on the inner and outer sides of the axial position inter-magnet ring for the rotor. The magnetic flux density map of $I_{Enhance}$ varying with distance when $I_z = 0$. The magnetic flux density map of I_z varying with distance when $I_{Enhance} = 0$.

As indicated by the red frame in Figure 9, the shielding ring separates the inner and outer air-gap regions. When the compensation winding carries zero current $I_{Enhance} = 0$ A, the axial flux density inside the shielding ring is nearly zero. As $I_{Enhance}$ increases, the internal axial air-gap flux density increases correspondingly. At $I_{Enhance} = 2$ A, the average flux density inside the shielding ring approximates the value outside the ring, indicating that the winding achieves its maximum boosting effect

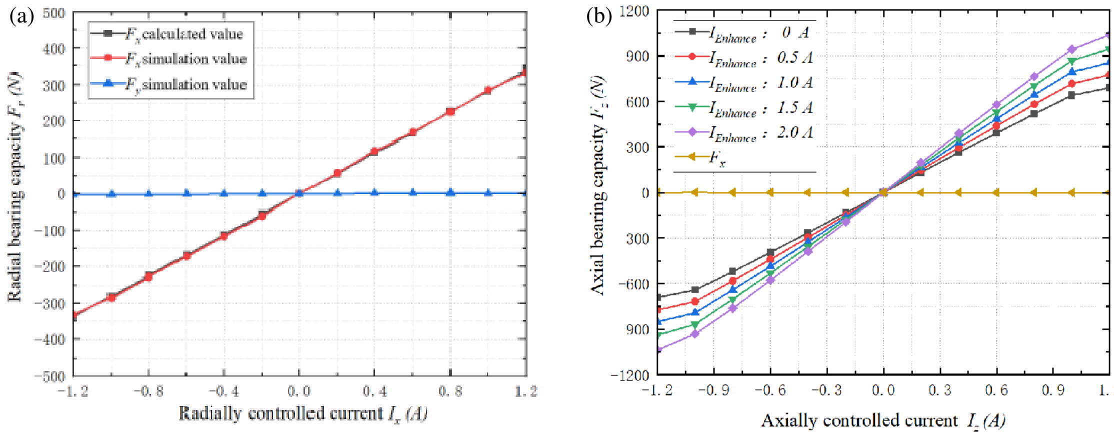

FIGURE 10. Relationship curve between suspension force and controlled current. (a) The relationship between radial suspension force and controlled current and (b) the relationship between axial suspension force and controlled current.

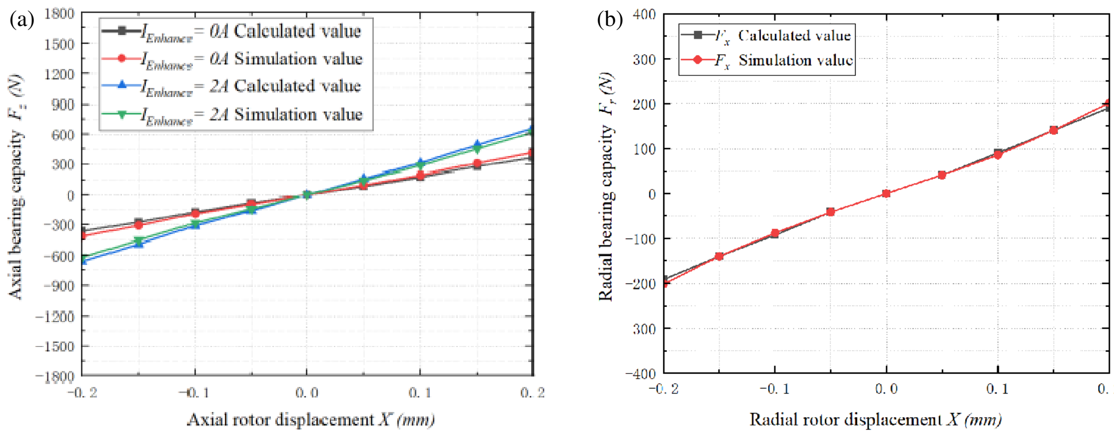

FIGURE 11. Relationship curve between suspension forces and rotor displacements. (a) Relationship between axial suspension forces and displacements and (b) relationship between radial suspension forces and displacements.

on the axial bias flux density. Given the design target of approximately 900 N controllable axial bearing capacity, $I_{Enhance}$ was set to 2 A to obtain a favorable control performance.

Figure 9 depicts the axial air-gap flux density distribution on the inner and outer sides of the rotor yoke under different axial control currents I_z, with $I_{Enhance} = 2$ A. For a given axial control current I_z, the air-gap flux density on the inner and outer sides of the rotor yoke is nearly identical, and its amplitude matches the design target. In addition, the variation trend in the air-gap flux density with varying currents is consistent with the theoretical design results.

4.3. Finite Element Analysis of 3 DOF-AEHMB

The core static characteristic of magnetic bearings refers to the correlation among bearing capacity, control current, and rotor displacement. In this section, the bearing capacity analytical formula derived in Section 3 and the 3D finite element method are adopted to plot the force-current and force-displacement characteristic curves of the proposed radial AEHMB.

Figure 10(a) illustrates the suspension forces versus radial control currents when the rotor is held at its equilibrium position. The suspension forces calculated from the analytical formula coincided well with the finite element simulation curves. The suspension forces exhibited an approximately linear relationship with control currents, whereas the Y-direction suspension force barely varied with changes in the X-direction control current.

Figure 10(b) shows suspension forces as a function of the axial control currents under the equilibrium rotor position. Multiple curves corresponding to different compensation winding currents $I_{Enhance}$ were plotted for comparison. When $I_{Enhance} = 2$ A, the maximum controllable axial suspension force reaches approximately 690 N at an axial control current of 1.2 A. In contrast, when $I_{Enhance} = 1.2$ A, the maximum controllable suspension force increases to 1040 N at the same axial control current of 1.2 A, representing a 51% improvement. This prominent enhancement effectively overcomes the limitation of insufficient axial load capacity inherent to conventional 3-DOF HMBs.

The characteristic curve maintains good linearity within the axial control current range of ± 1 A, where optimal control performance can be achieved. Once the axial control current exceeded 1 A, the curve slope gradually declined, indicating that the incremental gain in the bearing capacity per unit current diminished. For satisfactory operational efficiency, the axial control current should be limited to ± 1 A.

Figure 11(a) plots the axial suspension force versus axial displacement over the range of -0.2 mm to 0.2 mm. The axial suspension force exhibits an approximately linear relationship with axial displacement, and the analytical suspension force results agree well with the finite element simulation data. Energizing the bias current winding strengthens the axial magnetic flux, thus yielding a larger suspension force under identical rotor offset.

Figure 11(b) illustrates the radial suspension force as a function of radial displacement within -0.2 mm to 0.2 mm. Similarly, the radial suspension force varied linearly with radial displacement, and the analytical bearing-capacity calculations were consistent with the finite element simulations. Moreover, the matching degree between the analytical and simulated values was superior to that in the axial direction.

5. CONCLUSION

To address the proportional limitation between the axial and radial maximum suspension forces in the conventional 3-DOF HMBs, this study proposes a novel 3-DOF AEHMB. It introduces the structure of the 3-DOF AEHMB and the enhancement mechanism of its axial maximum suspension force. Based on the equivalent magnetic circuit method, mathematical models of axial and radial suspension forces were derived, and the design method for the main parameters is obtained. Then, based on the requirement that the ratio of the axial maximum suspension force to radial maximum suspension force is 4, the main parameters of the 3-DOF AEHMB were designed. The finite element method was adopted to verify the magnetic circuit, air-gap flux density, force-current relationship, and force-displacement relationship of this new 3-DOF AEHMB. The research results show that the structure, mechanism, mathematical model, and design method of this 3-DOF AEHMB are correct, enabling the free design of axial and radial maximum suspension forces.

ACKNOWLEDGEMENT

This work was supported in part by Major Projects of the Basic Science (Natural Science) Research Program in Jiangsu Higher Education Institutions (24KJA470002), and in part by Huaian City Key R&D Plan Projects (HAG202302).

REFERENCES

[1] Mancuzo, M. V., R. M. F. Neto, A. A. Cavallini Jr., and V. Steffen Jr., "Design and implementation of a low-cost active magnetic bearing," *Journal of Vibration Engineering & Technologies*, Vol. 12, No. 3, 2851–2864, 2024.

[2] Huang, Z., C. Li, Z. Zhou, B. Liu, Y. Zhang, M. Yang, T. Gao, M. Liu, N. Zhang, S. Sharma, Y. S. Dambatta, and Y. Li, "Magnetic bearing: Structure, model, and control strategy," *The International Journal of Advanced Manufacturing Technology*, Vol. 131, No. 5, 3287–3333, 2024.

[3] Laldingliana, J., S. Debnath, P. K. Biswas, and U. Das, "Design and speed control of U-type 3-coil active magnetic bearing," *Electrical Engineering*, Vol. 106, No. 2, 1135–1145, 2024.

[4] Yu, C., Y. Cai, W. Wang, W. Han, Z. Yin, and W. Han, "Analysis and compensation of Lorentz force magnetic bearing magnetic flux density uniformity error," *Sensors*, Vol. 24, No. 9, 2683, 2024.

[5] Li, B. and L. Zeng, "Position decoupling control of rigid rotor of active magnetic bearing," *Mechanika*, Vol. 29, No. 4, 292–301, 2023.

[6] Ahad, M. A. and S. M. Ahmad, "Marine rotor supported by frictionless 3-DOF active magnetic bearings," *Journal of Vibration Engineering & Technologies*, Vol. 13, No. 4, 254, 2025.

[7] Zhong, Y., L. Wu, Y. Fang, and X. Huang, "Investigation of cross-coupling effect of a 3-DOF magnetic bearing using magnetic circuit method," in *2017 20th International Conference on Electrical Machines and Systems (ICEMS)*, 1–6, Sydney, NSW, Australia, 2017.

[8] Sun, J., Z. Ju, C. Peng, Y. Le, and H. Ren, "A novel 4-DOF hybrid magnetic bearing for DGMSCMG," *IEEE Transactions on Industrial Electronics*, Vol. 64, No. 3, 2196–2204, 2017.

[9] Wu, L., D. Wang, Z. Su, K. Wang, and X. Zhang, "Analytical model of radial permanent magnet biased magnetic bearing with assist poles," *IEEE Transactions on Applied Superconductivity*, Vol. 26, No. 7, 1–5, 2016.

[10] Zhu, R., W. Xu, C. Ye, J. Zhu, G. Lei, and X. Li, "Design optimization of a novel heteropolar radial hybrid magnetic bearing using magnetic circuit model," *IEEE Transactions on Magnetics*, Vol. 54, No. 3, 1–5, 2018.

[11] Wang, Z., T. Zhang, and S. Wu, "Suspension force analysis of four-pole hybrid magnetic bearing with large radial bearing capacity," *IEEE Transactions on Magnetics*, Vol. 56, No. 8, 1–4, 2020.

[12] Singh, N. and P. K. Agarwal, "Self-tuned optimum control of hybrid foil magnetic bearing," *Journal of Vibration Engineering & Technologies*, Vol. 13, No. 6, 419, 2025.

[13] Boutra, N., R. Mehasni, and M. Feliachi, "Modeling and analysis of a proposed AC-DC C-core heteropolar radial hybrid magnetic bearing," *Applied Computational Electromagnetics Society Journal*, Vol. 39, No. 9, 814–822, 2024.

[14] Wu, M., H. Zhu, H. Zhang, and W. Zhang, "Modeling and multilevel design optimization of an AC-DC three-degree-of-freedom hybrid magnetic bearing," *IEEE Transactions on Industrial Electronics*, Vol. 70, No. 1, 233–242, 2023.

[15] Lu, J., Y. Yan, J. Ju, and H. Zhu, "Decoupling control of neural network inverse system based on improved online learning Levenberg-Marquardt for 3-DOF hybrid magnetic bearing," *Electrical Engineering*, Vol. 108, No. 1, 30, 2026.

[16] Wang, C., J. Fang, J. Tang, and J. Sun, "Structure and coupling analysis of a novel 3-DOF conical magnetic bearing," *International Journal of Applied Electromagnetics and Mechanics*, Vol. 43, No. 4, 389–401, 2013.

[17] Li, K. X., Z. Q. Deng, C. Z. Liu, *et al.*, "Design of disturbance rejection control system for 5-DOF magnetic bearing," *Journal of Aerospace Power*, Vol. 30, No. 4, 1016–1024, 2015.

[18] Sun, J. J., "Research on structure and design method of a new type of permanent magnet biased active magnetic bearing for magnetic levitation flywheel," Ph.D. dissertation, Beihang University, Beijing, China, 2012.

[19] Fang, J. C. and J. J. Sun, "New permanent magnet biased radial magnetic bearing in magnetic suspending flywheel application," *Journal of Beijing University of Aeronautics and Astronautics*, Vol. 32, No. 11, 1304–1307, 2006.

[20] Han, X., G. Liu, B. Chen, and S. Zheng, "Surge disturbance suppression of AMB-rotor systems in magnetically suspension centrifugal compressors," *IEEE Transactions on Control Systems Technology*, Vol. 30, No. 4, 1550–1560, 2022.

[21] He, J., Z. Deng, C. Peng, and K. Li, "Reduction of the high-speed magnetically suspended centrifugal compressor harmonic vibration using cascaded phase-shifted notch filters," *IEEE Sensors Journal*, Vol. 21, No. 2, 1315–1323, 2021.

[22] Uzhegov, N., A. Smirnov, C. H. Park, J. H. Ahn, J. Heikkinen, and J. Pyrhönen, "Design aspects of high-speed electrical machines with active magnetic bearings for compressor applications," *IEEE Transactions on Industrial Electronics*, Vol. 64, No. 11, 8427–8436, 2017.

[23] Filatov, A. and L. Hawkins, "Comparative study of axial/radial magnetic bearing arrangements for turbocompressor applications," *Proceedings of the Institution of Mechanical Engineers, Part I: Journal of Systems and Control Engineering*, Vol. 230, No. 4, 300–310, 2016.

[24] Han, B., Q. Xu, and Q. Yuan, "Multiobjective optimization of a combined radial-axial magnetic bearing for magnetically suspended compressor," *IEEE Transactions on Industrial Electronics*, Vol. 63, No. 4, 2284–2293, 2016.

[25] Zhong, Y., L. Wu, X. Huang, and Y. Fang, "Modeling and design of a 3-DOF magnetic bearing with toroidal radial control coils," *IEEE Transactions on Magnetics*, Vol. 55, No. 7, 1–7, 2019.

[26] Zhong, Y., L. Wu, Y. Fang, and X. Huang, "Investigation of cross-coupling effect and its restraining methods of a 3-DOF hybrid magnetic bearing," *COMPEL*, Vol. 37, No. 6, 2195–2210, 2018.

[27] Zhong, Y., L. Wu, X. Huang, Y. Fang, and J. Zhang, "An improved magnetic circuit model of a 3-DOF magnetic bearing considering leakage and cross-coupling effects," *IEEE Transactions on Magnetics*, Vol. 53, No. 11, 1–6, 2017.

[28] Le, Y., J. Sun, and B. Han, "Modeling and design of 3-DOF magnetic bearing for high-speed motor including eddy-current effects and leakage effects," *IEEE Transactions on Industrial Electronics*, Vol. 63, No. 6, 3656–3665, 2016.